RSC Advances

PAPER

View Article Online
View Journal | View Issue

Cite this: *RSC Adv.*, 2024, **14**, 32533

Photodynamic therapy of severe hemorrhagic shock on yolk–shell MoS_2 nanoreactors†

Yijun Zhang,‡[ab] Tianfeng Hua,‡[ab] Xiaoyi Huang,‡[cd] Rongrong Gu,[cd] Ruixi Chu,[cd] Yan Hu,[ab] Sheng Ye *[c] and Min Yang*[ab]

Received 6th June 2024
Accepted 7th August 2024

DOI: 10.1039/d4ra04157g

rsc.li/rsc-advances

Ischemia-reperfusion injury resulting from severe hemorrhagic shock continues to cause substantial damage to human health and impose a significant economic burden. In this study, we designed an Au-loaded yolk–shell MoS_2 nanoreactor (Au@MoS_2) that regulates cellular homeostasis. *In vitro* experiments validated the efficacy of the nanomaterial in reducing intracellular reactive oxygen species (ROS) production during hypoxia and reoxygenation, and had great cell biocompatibility, Au@MoS_2. The antioxidant properties of the nanoreactors contributed to the elimination of ROS (over twofold scavenging ratio for ROS). *In vivo* results demonstrate that Au@MoS_2 (54.88% of reduction) alleviates hyperlactatemia and reduces ischemia-reperfusion injury in rats subjected to severe hemorrhagic shock, compared to MoS_2 (26.32% of reduction) alone. In addition, no discernible toxic side effects were observed in the rats throughout the experiment, underscoring the considerable promise of the nanoreactor for clinical trials. The mechanism involves catalyzing the degradation of endogenous lactic acid on the Au@MoS_2 nanoreactor under 808 nm light, thereby alleviating ischemia-reperfusion injury. This work proposes a new selective strategy for the treatment of synergistic hemorrhagic shock.

1 Introduction

Severe hemorrhagic shock (SHS) is a type of hypovolemic shock characterized by a blood volume loss greater than 40% of the total blood volume.[1] This acute volume loss leads to inadequate tissue and organ perfusion, resulting in a decreased oxygen delivery to cells.[2] Despite advances in medical technology and improvements in diagnostic and therapeutic approaches, the morbidity and mortality rates associated with hemorrhagic shock remain high, making it a significant contributor to mortality in critically ill patients.[3] Successful resuscitation requires prompt intervention, including timely hemostasis and rehydration therapy, to reduce tissue oxygen debt and thereby prevent cell necrosis and apoptosis.[4] However, recent studies increasingly suggest that the "second blow" induced by ischemia-reperfusion injury and the subsequent immunoinflammatory cascade may pose a greater threat to such patients.[5] Hemorrhagic shock involves oxygen kinetic dysfunction in its pathophysiology. In cases of inadequate oxygen delivery, cellular aerobic oxidation is converted to anaerobic oxidation, leading to the accumulation of substantial lactic acid in the body.[6,7] This lactic acid accumulation triggers pro-inflammatory signals and increases the production of reactive oxygen species (ROS).[5] While moderate levels of ROS are critical for intracellular signaling and defense against pathogens, excessive ROS overwhelm cellular antioxidants and cause extensive cell damage, including organelle destruction, cell membrane rupture, and DNA damage.[8] Therefore, addressing ROS is crucial for mitigating ischemic-reperfusion injuries associated with hemorrhagic shock.

In recent years, the field of nanomedicine has experienced rapid development, resulting in the creation of unique antioxidants with exceptional ROS scavenging capabilities for the treatment of ROS-related diseases such as stroke, neurodegeneration, atherosclerosis, and diabetes.[9–12] Nevertheless, therapeutic efficacy is often limited by the inability to precisely target drugs to affected areas and the non-specific modulation of autoimmune cells.[13–15] Achieving precise delivery and controlled release of reducing agents will be critical to enhance the therapeutic potential of antioxidant nanomaterials.[16–19] Recent research suggests an innovative strategy using reducing chemical factors in disease microenvironments, such as tumors and diabetes, as sacrificial agents for artificial catalysts. This aims to achieve sustainable and controllable substrate

[a]*The Second Department of Critical Care Medicine, The Second Affiliated Hospital of Anhui Medical University, Hefei, Anhui 230001, China. E-mail: yangmin@ahmu.edu.cn*

[b]*Laboratory of Cardiopulmonary Resuscitation and Critical Care, The Second Affiliated Hospital of Anhui Medical University, Hefei, Anhui 230001, China*

[c]*School of Materials and Chemistry, Anhui Agricultural University, Hefei, Anhui 230036, China. E-mail: sye503@ahau.edu.cn*

[d]*College of Animal Science and Technology, Anhui Agricultural University, Hefei, Anhui 230036, China*

† Electronic supplementary information (ESI) available. See DOI: https://doi.org/10.1039/d4ra04157g

‡ These authors contributed equally to this work.

consumption *via* the photocatalytic pathway, thereby enhancing therapeutic efficacy.[20–23] For example, Zhao *et al.* have pioneered a photocatalysis-mediated Z-scheme $SNS_{1.68}$–$WO_{2.41}$ nanoreactor capable of generating hydrogen gas by utilizing the excess glutathione in tumors.[23] This disrupts the redox balance within tumors, induces apoptosis, and demonstrates remarkable therapeutic efficacy and biosafety. Similarly, Chen *et al.* discuss hydrogen-doped titanium oxide nanorods (HTON) using glucose as a sacrificial agent for visible light catalytic therapy. Glucose modulates the levels of advanced glycation end products (AGEs) and their receptor (RAGE) during oxidation, mitigates skin cell apoptosis, and improves diabetic wound healing.[20] These findings suggest that the consumption of endogenous lactate may also have the potential to ameliorate ischemia-reperfusion injury resulting from hemorrhagic shock. This dual regulation-reducing ROS-induced oxidative stress and controlling lactate accumulation *in vivo*-offers a promising therapeutic avenue for mitigating ischemia-reperfusion injury.

Molybdenum is a vital dietary trace element that is essential for human survival.[24,25] Molybdenum-containing enzymes play pivotal roles in various metabolic processes in the human body, including those catalyzed by xanthine oxidase, aldehyde oxidase, and sulfite oxidase.[26] Recently, MoS_2 nanomaterials have gained increasing prominence in the field of disease diagnosis and treatment due to their remarkable properties, including facile controllable synthesis, a substantial specific surface area, ease of biomolecular functionalization, and compatibility with various nanoreactors.[27–35] MoS_2 exhibits exceptional optical absorption and remarkable photothermal conversion efficiency in the near-infrared (NIR) range, making it suitable for photodynamic therapy.[12,36–39] Numerous studies have demonstrated that MoS_2 nanosheets can efficiently eliminate various ROS due to their inherent peroxidase (POD) activity. In addition, molybdenum disulfide is capable of scavenging other free radicals, such as $^{\bullet}OH$ and $^{\bullet}DPPH$.[40–43]

In this study, a yolk–shell Au@MoS_2 nanoreactor was synthesized to regulate intracellular environmental homeostasis. Photodynamic therapy is used to decrease endogenous lactic acid production, thereby ameliorating ischemia-reperfusion injury associated with hemorrhagic shock. This innovative method represents a clinically relevant approach to the treatment of hemorrhagic shock.

2 Experimental

2.1 Synthesis of yolk–shell MoS_2

The initial formulation involved dissolving 0.2420 g of molybdate and 0.6 g of glucose in distilled water. This set the foundation for the experiment. Additionally, a second compound was prepared by mixing 5.4650 g of cetyltrimethyl ammonium bromide (CTAB) with 100 mL of *n*-butanol. The second compound was then added to the initial solution, and the mixture was stirred for 2 hours. Subsequently, 50 mL of glycol and 0.8 mL of hydrochloric acid were added and stirred. Following this, 1.1420 g of thiourea was introduced, and the mixture was stirred for an additional 3 hours. The resulting solution was then transferred to a polytetrafluoroethylene reactor for a hydrothermal reaction, followed by vacuum drying, calcined in a tube furnace (Anhui Kemei Machinery Technology Co., Ltd), resulting in the formation of yolk–shell MoS_2. The third formulation was prepared by combining 1.21 mL of gold (Au) solution and 0.08 g of dioctyl sulfosuccinate sodium salt (AOT) in distilled water. The fourth compound was formed through the addition of 80 mg of yolk–shell MoS_2 to a solution containing 36 mL of ethanol and 12 mL of distilled water. This step established the basis for subsequent reactions. Following this, the third compound, along with 0.4 g of L-ascorbic acid, was introduced into the mixture for the fourth compound, and the combined solution was stirred continuously for 12 hours. The final product, yolk–shell Au@MoS_2, was synthesized through a 12 hours hydrothermal reaction of the resultant solution.

2.2 *In vitro* biocompatibility

To evaluate the biocompatibility of the new material, we conducted *in vitro* experiments using rat cardiomyocytes (H9c2). H9c2 cells, originally derived from rat embryonic cardiomyocytes obtained from the Chinese Type Culture Collection Center of Wuhan University, were cultured in medium supplemented with 10% fetal bovine serum (LONSERA) and 1% penicillin–streptomycin (Beyotime Biotechnology). The cells were maintained in a 37 °C incubator with 5% CO_2 and the medium was changed every 2 days. Logarithmically growing H9c2 cardiomyocytes were used for the CCK-8 experiment. Before the experiment, cells were washed twice with PBS, digested with pancreatic enzymes, centrifuged at 1000 rpm, and re-suspended. Cell counting was performed after resuspension using a cell counting plate, where the number of cells in suspension was calculated as (total number of cells in four squares on the counting plate/4) $\times 10^4 \times$ dilution factor $\times$ volume. The cell concentration was adjusted to approximately 8000 cells per well in a 96-well plate for subsequent experiments. Initially, various concentrations of MoS_2 (10 μg mL^{-1}) were deposited onto a 96-well culture plate, and subsequently, recovered H9c2 cells were seeded and incubated at 37 °C overnight. After 48 hours, the cell culture was refreshed with medium containing CCK-8 test solution After 2 hours incubation, we measured the absorbance to calculate cell viability. Additionally, *in vitro* hemolysis experiments were performed using red blood cells from healthy Sprague-Dawley (SD) rats to evaluate the hemolytic properties of Au@MoS_2. Initially, whole blood from healthy SD rats was collected in an anticoagulant tube, centrifuged at 3000 rpm for 20 minutes, and the resulting red blood cells were separated after serum removal. Different concentrations of Au@MoS_2 were then prepared, and 1 mL of Au@MoS_2 solutions, along with 1 mL of PBS and 1 mL of ultrapure water, were each placed in separate EP tubes. Finally, the hemolysis rate was determined by measuring the absorbance of the supernatant after centrifugation.

2.3 Intracellular ROS determination

We assessed ROS levels using the non-fluorescent probe dichlorofluorescein diacetate (DCFH-DA). H9c2 cells were seeded in 6-well plates and subjected to anoxic treatment in a chamber containing 99% nitrogen and 1% oxygen following

24 hours of growth. The concentration of MoS_2 added is 10 μg mL^{-1}. After 1 hour of reoxygenation, the cells were incubated with DCFH-DA at 37 °C for 30 minutes. The distribution of DCF fluorescence was subsequently detected at 535 nm using a fluorescence microscope.

2.4 Hemorrhagic shock test *in vivo*

In our study, we conducted *in vivo* experiments using SD rats to evaluate the material's effectiveness. All animal procedures were ethically approved by the Animal Experiment Ethics Committee. The rats fasted for 12 hours prior to anesthesia but had access to water. CO_2 was employed for pre-anesthesia induction, and after induction, the abdomen, neck, and right groin were sterilized with iodine and alcohol. An intraperitoneal injection of 3% pentobarbital solution provided abdominal anesthesia, with additional maintenance doses administered hourly. Following anesthesia, a tracheotomy was performed to facilitate unrestricted breathing. A longitudinal incision was made in the right inguinal ligament direction, and the right femoral arteriovenous was exposed. A PE50 tube was inserted into the arteriovenous, and the femoral arterial catheter was connected to a physiological monitor for recording mean arterial pressure (MAP) and heart rate, as well as monitoring blood gases. A femoral vein catheter was utilized for intraoperative fluid, blood transfusion, and drug administration, while the right internal carotid artery was catheterized for controlled bleeding. After completing these procedures, a 20 minutes stabilization period was observed and recorded as the Baseline. Prior to blood collection in all groups, heparinization was performed, and blood was withdrawn through the right femoral vein. Approximately 40% of the total blood volume of the rats was extracted at a constant rate through the right internal carotid artery to induce severe shock, followed by maintaining MAP between 30 ± 5 mmHg through repeated blood withdrawal or minor back transfusion. Rats in the material group received injections in the right lower abdomen and were then exposed to 808 nm light irradiation for 40 minutes. The light dose of NIR is 366.97 J cm^{-2} and the light intensity of NIR is 275.52 J. Extracted blood was refrigerated at 4 °C and removed 10 minutes before resuscitation, subsequently being rewarmed to room temperature. At the commencement of resuscitation, except for the sham group, all other groups received a continuous-rate injection through the right femoral vein using a microinjection pump over 40 minutes. Following resuscitation, anesthesia was sustained for 3 hours, after which euthanasia was carried out.

3 Results and discussion

3.1 Preparation and characterization of yolk–shell MoS_2

The yolk–shell MoS_2 and Au@MoS_2 were synthesized using a hydrothermal method involving sodium molybdate in

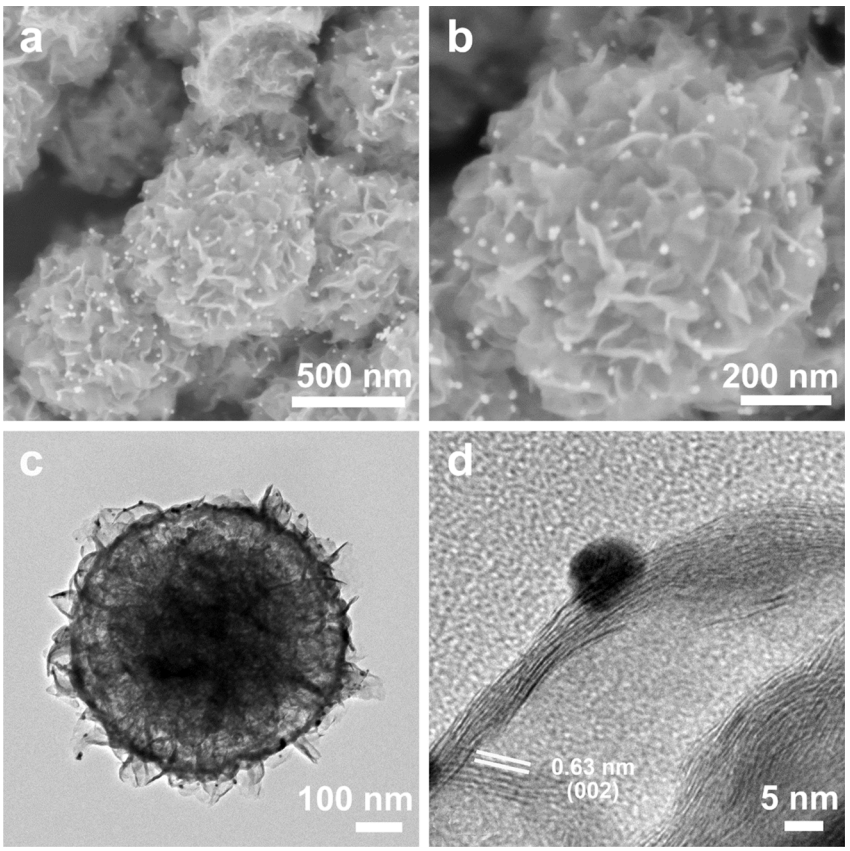

Fig. 1 SEM images at different magnifications of the yolk–shell Au@MoS_2 (a and b). TEM images at different magnifications of yolk–shell Au@MoS_2 (c and d). SEM: scanning electron microscope. TEM: transmission electron microscopy.

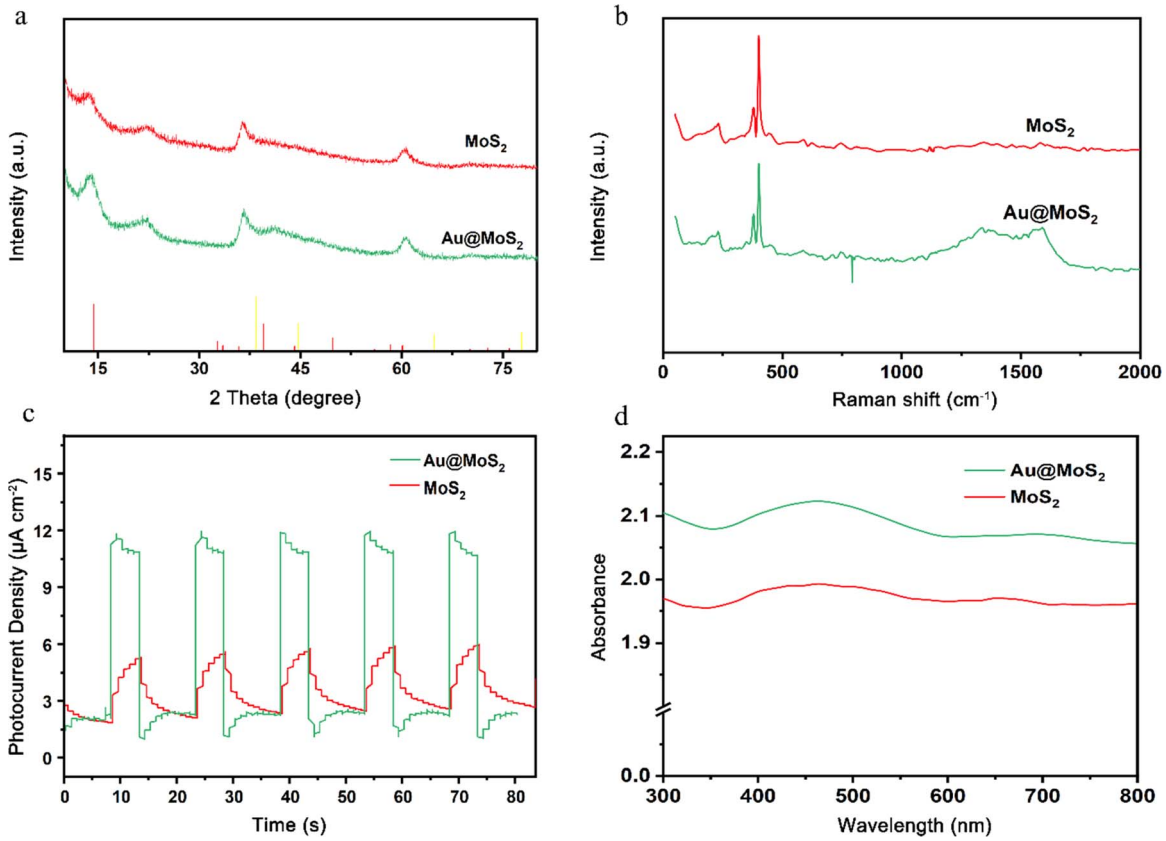

Fig. 2 X-ray diffraction (a), Raman spectroscopy (b), photocurrent testing (c), and ultraviolet spectroscopy (d) were conducted on MoS_2 and Au@MoS_2.

a thiourea-mixed solution as the sulfur source (Fig. S1†). The scanning electron microscopy (SEM) images reveal that Au@MoS_2 nanospheres display a yolk–shell morphology with a diameter of 650 nm (Fig. 1a and b). The transmission electron microscopy (TEM) images demonstrated the uniform yolk–shell structure of both MoS_2 and Au@MoS_2 (Fig. S2 and S3†). High-resolution transmission electron microscopy (HRTEM) revealed uniformly attached Au nanoparticles with a diameter of approximately 10 nm on the surface of MoS_2 (Fig. 1c and d).

MoS_2 and yolk–shell Au@MoS_2 nanomaterials were prepared and characterized using X-ray diffraction (XRD) and Raman spectroscopy. Examination of the XRD pattern and Raman spectrogram reveals that the peak shape of Au nanoparticles remains largely consistent before and after loading. Additionally, all diffraction peaks correspond well to MoS_2, and the intrinsic properties of the material remain unaltered during the Au particle loading process (Fig. 2a and b). The photocurrent–time curve was generated using the chronoamperometric method under Xenon lamp source (PLS-SXE300+), as depicted in Fig. 2c. The photocurrent density of yolk–shell Au@MoS_2 surpasses that of yolk–shell MoS_2, signifying a substantially higher efficiency in the separation of electron–hole pairs in yolk–shell Au@MoS_2. Furthermore, in the UV absorption spectrum, yolk–shell Au@MoS_2 displayed a broader light absorption range compared to yolk–shell MoS_2 (Fig. 2d). Electrochemical impedance spectroscopy (EIS) is a powerful tool for studying charge transfer resistance at electrolyte/semiconductor interfaces. The smaller diameter of Au@MoS_2 compared to MoS_2 implies lower charge transfer resistance (Fig. S4†). To summarize, yolk–shell Au@MoS_2 demonstrates remarkable advantages in charge separation and transfer and displays a broader photoabsorption range compared to yolk–shell MoS_2.

Fourier transform infrared (FT-IR) was used to characterize the chemical structures of MoS_2 and Au@MoS_2. FT-IR can be used to study and identify the structure and composition of materials. Two strong absorption peaks of Au@MoS_2 and MoS_2 can be observed at 2920–2850 cm^{-1}, which can be attributed to

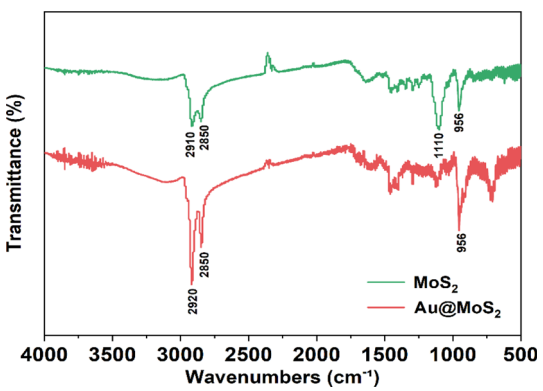

Fig. 3 FT-IR of yolk–shell Au@MoS_2.

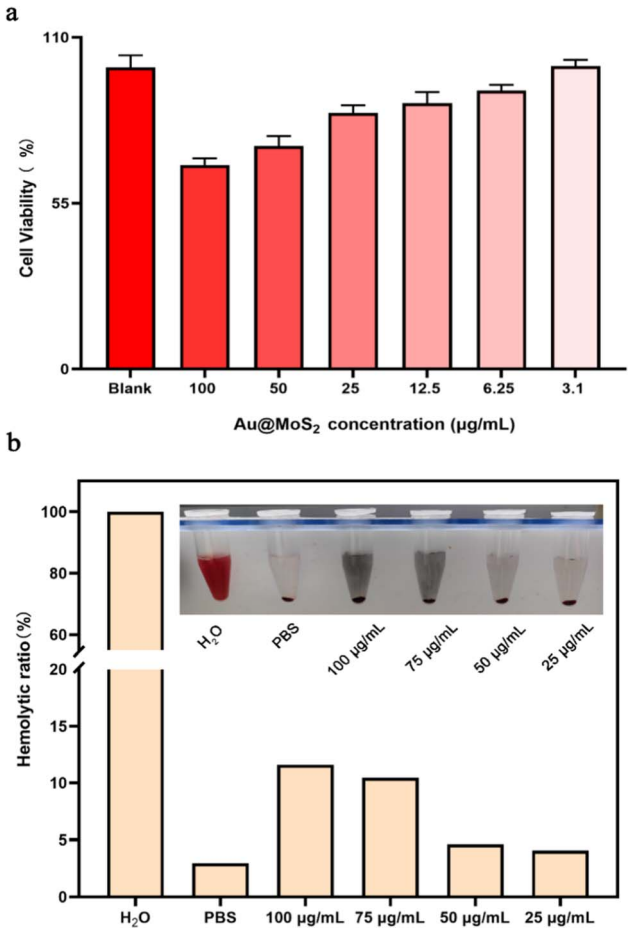

Fig. 4 The safety of MoS_2 *in vitro*. (a) Cells viabilities of H9c2 after cultured with different concentrations of Au@MoS_2. (b) Hemolysis ratio of red blood cells incubated with Au@MoS_2 and the photographs of red blood cells after centrifugation in set. We observed cell morphology from *in vitro* cytocompatibility studies. In the range of 50–100 μg per mL Au@MoS_2, the morphology of some cells changed from long spindle-shaped to round, and some apoptotic cells were observed. At concentrations below 50 μg mL^{-1}, the cell morphology remained basically unchanged (Fig. 5).

the stretching vibration of $–CH_2–$. The peak value at 1110 cm^{-1} is related to the stretching vibration of C–O. The peak at 956 cm^{-1} is attributed to the bending vibration of some H-containing groups. The surface Au was successfully loaded on MoS_2 by FT-IR test (Fig. 3).

3.2 *In vitro* biocompatibility

To ensure the safe application of Au@MoS_2 material in animal experiments, we performed preliminary *in vitro* biocompatibility evaluations. H9c2 cells were chosen for co-culture treatment, and their activity was subsequently assessed using the CCK-8 assay. The results indicate that cell activity is minimally affected when the MoS_2 concentration is maintained below 12.5 μg mL^{-1}. However, concentrations above 25 μg mL^{-1} correlate with a decrease in cell viability (Fig. 4a). To further investigate the blood compatibility of MoS_2, we incubated SD rat red blood cells for 2 hours and analyzed the absorbance of the supernatant. The figure illustrates that a significant number of red blood cells were lysed in the ultra-pure water group, with a hemolysis rate of 100% in this group. When PBS and various concentrations of MoS_2 were introduced, fewer red blood cells experienced lysis, resulting in hemolysis rates generally below 5% (Fig. 4b). Considering these findings, we selected a MoS_2 concentration of 10 μg mL^{-1}.

3.3 ROS production *in vitro*

In the experimental setup, Au@MoS_2 catalyzes the intracellular consumption of lactate, leading to a diminished generation of ROS. For this study, we utilized H9c2 cells in a hypoxia-reoxygenation experiment, incorporating MoS_2 and 808 nm light irradiation as interventions. The figure demonstrates that the application of Au@MoS_2 significantly decreased intracellular ROS production in H9c2 cells following 12 hours of hypoxia, as compared to the control group. These findings highlight the pronounced ROS scavenging effect of Au@MoS_2 in response to the increased ROS levels induced by hypoxia and reoxygenation (Fig. 6a and b).

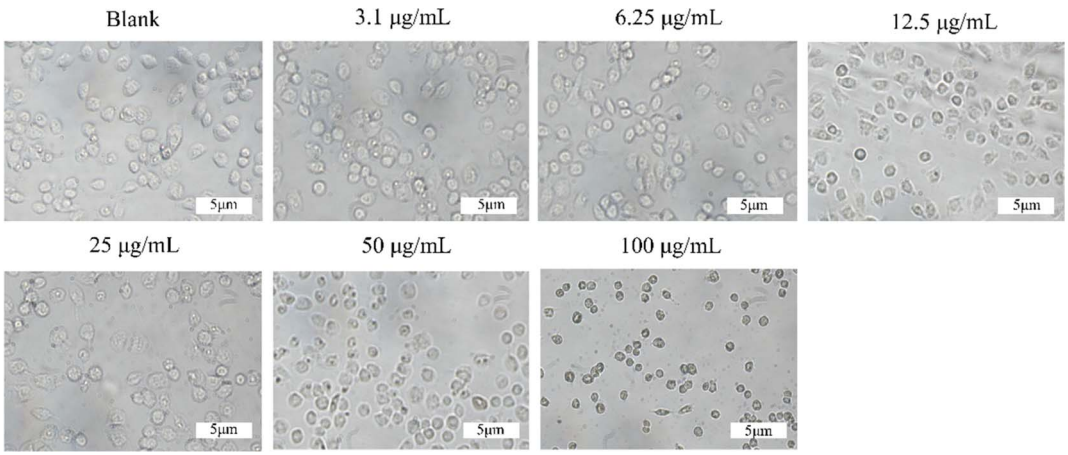

Fig. 5 Cell morphology at different concentrations of Au@MoS_2.

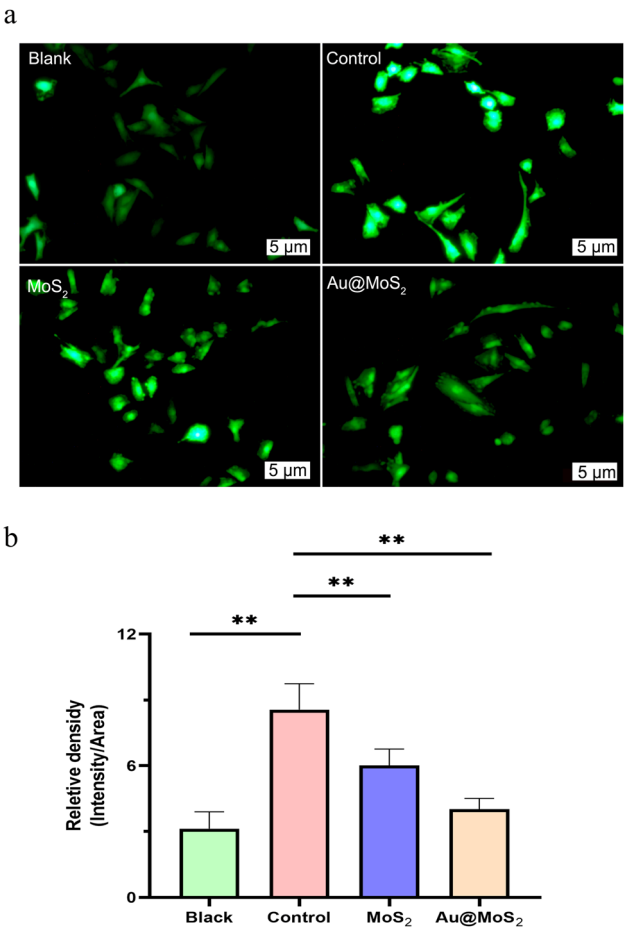

Fig. 6 Comparison of intracellular ROS fluorescence images (a) and fluorescence intensity (b) by MoS_2 intervention.

3.4 Hemorrhagic shock experiment

To assess the effectiveness of our material in treating hyperlactatemia, we created hemorrhagic shock models in rats. As illustrated in the Fig. 7, we administered a 1 mL injection of MoS_2 (10 mg mL^{-1}) into the right lower abdomen after withdrawing 40% of the rats' total blood volume, followed by 40 minutes of 808 nm light irradiation. Subsequently, after reinfusing the withdrawn blood, we monitored the rats' vital signs and arterial blood gas levels for a duration of 3 hours.

Prior to infusion, no significant differences were observed among groups in MAP, lactic acid (Lac), base excess (BE), or potential of hydrogen (pH). As blood was continuously withdrawn, all rat groups, except the sham group, exhibited a consistent response to bleeding. Specifically, Lac and pH levels began to gradually rise, while BE and MAP decreased. Following a 40% blood withdrawal, the MAP for rats in the Control and MoS_2 groups stabilized at approximately 30 mmHg during the maintenance of hemorrhagic shock. Over time, Lac levels in the rats' blood increased during shock, while pH and BE decreased, indicating the potential occurrence of metabolic acidosis. Blood gas indices in all groups exhibited a consistent trend of change, but the indices in rats following MoS_2 intervention displayed a milder alteration. At the 40 minutes mark of shock, the alterations in Lac, BE, and pH in rats from all groups exhibited statistically significant differences ($P < 0.05$). Notably, the Lac levels in rats treated with $Au@MoS_2$ consistently remained at a low level, and the MoS_2 group also exhibited some inhibitory effects on Lac increase compared to the control group. Through the continuous transfusion of their own blood, the MAP and BE levels in the rats rose rapidly, eventually returning to baseline. As resuscitation time extended, Lac levels continuously decreased, BE and pH increased gradually, and the heart rate of the rats gradually stabilized. The results suggested that rats in all groups had gradually recovered from hemorrhagic shock. The application of $Au@MoS_2$ proves effective in mitigating lactic acidosis among rats experiencing hemorrhagic shock. Additionally, its combination with blood transfusion therapy accelerates the restoration of the body to a normal state, demonstrating significant potential in treating ischemia-reperfusion injury resulting from hemorrhagic shock (Fig. 8a–d).

3.5 Photocatalytic mechanism

Drawing upon the aforementioned experimental results, we formulated a hypothesis regarding the potential mechanism through which $Au@MoS_2$ facilitates substrate lactate reduction.

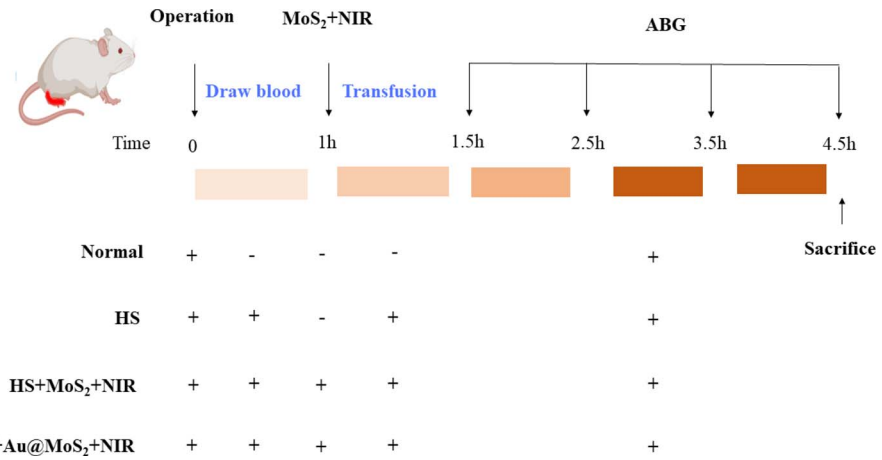

Fig. 7 Hemorrhagic shock model establishment and grouping diagram. ABG: arterial blood gases, HS: hemorrhagic shock, NIR: near infrared.

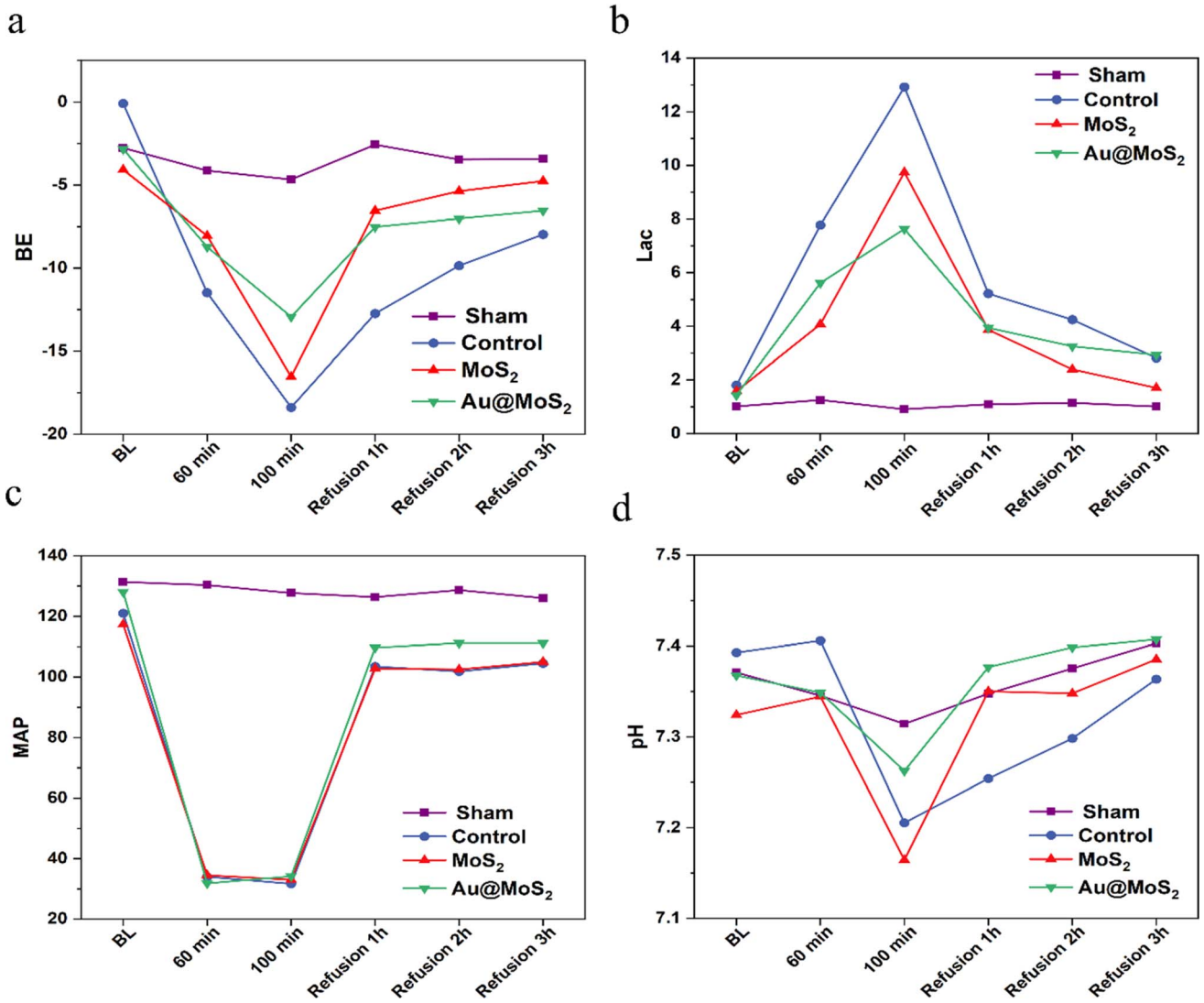

Fig. 8 The trends in BE (a), Lac (b), MAP (c), and pH (d) among rats in hemorrhagic shock. BE: base excess, Lac: lactic acid, MAP: mean arterial pressure, pH: potential of hydrogen.

MoS_2, serving as a light-trapping semiconductor material, generally follows three basic steps in its photodynamic therapy principle:

$$MoS_2 + hv \rightarrow e^-(MoS_2) + h^+(MoS_2) \quad (1)$$

$$CH_3CHCOOH + 2h^+ \rightarrow CO_2 + H_2O \quad (2)$$

$$A + e^- \rightarrow A^- \quad (3)$$

In the equation above, MoS_2, functioning as a light-trapping semiconductor material, generates electron–hole pairs upon photoexcitation. These photogenerated electrons and holes are subsequently separated and migrate to the surface of the MoS_2 semiconductor. Photogenerated electrons transfer from the conduction band MoS_2 to Au nanoparticles, promoting charge separation of yolk–shell MoS_2 nanoreactor. The lactic in cell tissue is oxidized and consumed by the photogenerated holes. Concurrently, the photogenerated electrons engage in a reaction with A(acceptor) to generate A^- (Fig. 9). Accordingly, it alleviates the acidic microenvironment during hemorrhagic shock and reduces oxidative stress during resuscitation.

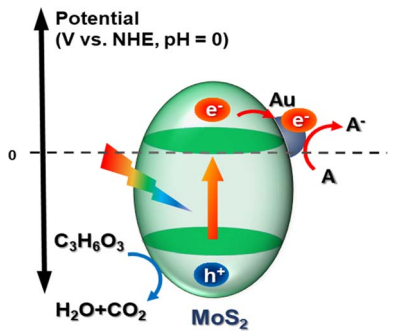

Fig. 9 Principle of phototherapy with MoS_2 nanoreactor.

4 Conclusions

In conclusion, we have synthesized yolk–shell MoS_2 nanospheres coated with Au nanoparticles to facilitate the photocatalytic treatment of severe hemorrhagic shock. *In vitro* biocompatibility studies reveal that yolk–shell MoS_2 nanospheres exhibit high safety, low cytotoxicity, and excellent biocompatibility. *In vivo* experiments in rats confirmed that augmenting Au-coated MoS_2 nanomaterials has a more pronounced impact on hyperlactatemia resulting from hemorrhagic shock in the near-infrared range, compared to yolk–shell MoS_2 nanoparticles. Our study introduces a novel approach for the treatment of ischemia-reperfusion injury after hemorrhagic shock, which has significant clinical application value. However, our research still has limitations. First, the majority of our studies are qualitative, with a notable absence of quantitative analyses to elucidate the dose–response relationship. Second, the sample size in our experimental studies is limited; therefore, larger-scale investigations are warranted to comprehensively determine the protective mechanisms and effects of Au@MoS_2 in hemorrhagic shock.

Ethics approval and consent to participate

The animal experimental processes were approved by the Ethnic Committee of Anhui Medical University (Ethical Number: LLSC20211456) and conducted in strict accordance to the standard of the Guide for the Care and Use of Laboratory Animals published by the Ministry of Science and Technology of the People's Republic of China in 2006. All experimental animals were purchased from Jinan Pengyue Experimental Animal Breeding Co., Ltd.

Data availability

The data supporting this article have been included as part of the ESI.†

Author contributions

Yijun Zhang: conceptualization, data curation, investigation, methodology, writing – original draft; Tianfeng Hua: data curation, investigation, methodology, writing – original draft; Xiaoyi Huang: data curation, investigation, methodology, writing – original draft; Rongrong Gu: data curation, investigation; Ruixi Chu: data curation, investigation, methodology, writing – original draft; Yan Hu: data curation, investigation; Sheng Ye: funding acquisition, supervision; Min Yang: funding, acquisition, supervision.

Conflicts of interest

The authors declare that they have no known competing financial interests or personal relationships that could have appeared to influence the work reported in this paper.

Acknowledgements

This work was financially supported by the National Natural Science Foundation of China (22372001), Starting Fund for Scientific Research of High-Level Talents, Anhui Agricultural University (rc382108), the Open Fund of the State Key Laboratory of Molecular Reaction Dynamics in DICP, CAS (SKLMRD-K202223), the Key Research Project of the Natural Science Foundation of Anhui Provincial Universities (KJ2023AH050997), Innovation and entrepreneurship training program for college students, Anhui Agricultural University (G202210364445, S202210364091, X202210364528), Research Fund of Anhui Institute of Translational Medicine (2022zhyx-C76) and Postgraduate Innovation Research and Practice Program of Anhui Medical University (YJS20230085). Thank Dr Qin Wang and Dr Yang Xu from the Biotechnology Center of Anhui Agricultural University for their help on material characterization in this work.

References

1 J. W. Cannon, *N. Engl. J. Med.*, 2018, **378**, 370–379.
2 H. Lier, M. Bernhard and B. Hossfeld, *Anaesthesist*, 2018, **67**, 225–244.
3 B. J. Eastridge, J. B. Holcomb and S. Shackelford, *Transfusion*, 2019, **59**, 1423–1428.
4 D. Salvemini and S. Cuzzocrea, *Free Radical Biol. Med.*, 2002, **33**, 1173–1185.
5 A. Panisello-Roselló and J. Roselló-Catafau, *Int. J. Mol. Sci.*, 2018, **19**, 31.
6 K. J. Gunnerson, M. Saul, S. He and J. A. Kellum, *Crit. Care*, 2006, **10**, R22.
7 P. Zhai, S. Sciarretta, J. Galeotti, M. Volpe and J. Sadoshima, *Circ. Res.*, 2011, **109**, 502–511.
8 H. K. Eltzschig and C. D. Collard, *Br. Med. Bull.*, 2004, **70**, 71–86.
9 N. Kamimura, K. Nishimaki, I. Ohsawa and S. Ohta, *Obesity*, 2011, **19**, 1396–1403.
10 H. Shiroto, H. Tomita, J. Hagii, N. Metoki, A. Fujita, T. Kamada, K. Takahashi, S. Saito, S. Sasaki, H. Hitomi, S. Seino, Y. Baba, T. Uchizawa, M. Iwata, S. Matsumoto, M. Yasujima and K. Okumura, *J. Stroke Cerebrovasc. Dis.*, 2018, **27**, 276.
11 X. Tan, F. Shen, W. L. Dong, Y. Yang and G. Chen, *Med. Gas Res.*, 2018, **8**, 176–180.
12 X. Zhai, X. Chen, J. Shi, D. Shi, Z. Ye, W. Liu, M. Li, Q. Wang, Z. Kang, H. Bi and X. Sun, *Free Radical Biol. Med.*, 2013, **65**, 731–741.
13 E. A. Lepeltier, L. Nuhn, C. M. Lehr and R. Zentel, *Nanomedicine*, 2015, **10**, 3147–3166.
14 B. B. Mendes, D. P. Sousa, J. Conniot and J. Conde, *Trends Cancer*, 2021, **7**, 847–862.
15 Y. Zhao, P. Yue, Y. Peng, Y. Sun, X. Chen, Z. Zhao and B. Han, *Drug Delivery*, 2023, **30**, 1–18.
16 D. Fan, Y. Cao, M. Cao, Y. Wang, Y. Cao and T. Gong, *Signal Transduction Targeted Ther.*, 2023, **8**, 293.

17 K. Fan, C. Cao, Y. Pan, D. Lu, D. Yang, J. Feng, L. Song, M. Liang and X. Yan, *Nat. Nanotechnol.*, 2012, **7**, 459–464.
18 M. Huo, L. Wang, Y. Chen and J. Shi, *Nat. Commun.*, 2017, **8**, 357.
19 H. Lin, Y. Chen and J. Shi, *Chem. Soc. Rev.*, 2018, **47**, 1938–1958.
20 S. Chen, Y. Zhu, Q. Xu, Q. Jiang, D. Chen, T. Chen, X. Xu, Z. Jin and Q. He, *Nat. Commun.*, 2022, **13**, 5684.
21 G. Tao, F. Liu, Z. Jin, B. Liu, H. Wang, D. Li, W. Tang, Y. Chen, Q. He and S. Qin, *Theranostics*, 2023, **13**, 2455–2470.
22 Y. Xu, M. Fan, W. Yang, Y. Xiao, L. Zeng, X. Wu, Q. Xu, C. Su and Q. He, *Adv. Mater.*, 2021, **33**, e2101455.
23 B. Zhao, Y. Wang, X. Yao, D. Chen, M. Fan, Z. Jin and Q. He, *Nat. Commun.*, 2021, **12**, 1345.
24 M. Liu, C. Zhang, A. Han, L. Wang, Y. Sun, C. Zhu, R. Li and S. Ye, *Nano Res.*, 2022, **15**, 6862–6887.
25 M. Zhu, X. Liu, L. Tan, Z. Cui, Y. Liang, Z. Li, K. W. Kwok Yeung and S. Wu, *J. Hazard. Mater.*, 2020, **383**, 121122.
26 L. Zhu, Y. Zhang, P. Xu, W. Wen, X. Li and J. Xu, *Biosens. Bioelectron.*, 2016, **80**, 601–606.
27 B. Balan, M. M. Xavier and S. Mathew, *ACS Omega*, 2023, **8**, 25649–25673.
28 W. Cao, L. Yue and Z. Wang, *Carbohydr. Polym.*, 2019, **215**, 226–234.
29 N. Dhas, R. Kudarha, A. Garkal, V. Ghate, S. Sharma, P. Panzade, S. Khot, P. Chaudhari, A. Singh, M. Paryani, S. Lewis, N. Garg, N. Singh, P. Bangar and T. Mehta, *J. Controlled Release*, 2021, **330**, 257–283.
30 Z. Feng, X. Liu, L. Tan, Z. Cui, X. Yang, Z. Li, Y. Zheng, K. W. K. Yeung and S. Wu, *Small*, 2018, **14**, e1704347.
31 M. Liu, J. Zhu, Y. Liu, F. Gong, R. Li, H. Chen, M. Zhao, Q. Jiang, J. Liu and S. Ye, *Chem. Eng. J.*, 2022, **446**, 137080.
32 M.-Y. Peng, D.-W. Zheng, S.-B. Wang, S.-X. Cheng and X.-Z. Zhang, *ACS Appl. Mater. Interfaces*, 2017, **9**, 13965–13975.
33 Q. H. Wang, K. Kalantar-Zadeh, A. Kis, J. N. Coleman and M. S. Strano, *Nat. Nanotechnol.*, 2012, **7**, 699–712.
34 S. Ye, W. Shi, Y. Liu, D. Li, H. Yin, H. Chi, Y. Luo, N. Ta, F. Fan, X. Wang and C. Li, *J. Am. Chem. Soc.*, 2021, **143**, 12499–12508.
35 Z. Yuan, B. Tao, Y. He, J. Liu, C. Lin, X. Shen, Y. Ding, Y. Yu, C. Mu, P. Liu and K. Cai, *Biomaterials*, 2019, **217**, 119290.
36 Z. Liang, R. Shen, Y. H. Ng, P. Zhang, Q. Xiang and X. Li, *J. Mater. Sci. Technol.*, 2020, **56**, 89–121.
37 Y. H. Wang, K. J. Huang and X. Wu, *Biosens. Bioelectron.*, 2017, **97**, 305–316.
38 S. Ye, C. Ding, R. Chen, F. Fan, P. Fu, H. Yin, X. Wang, Z. Wang, P. Du and C. Li, *J. Am. Chem. Soc.*, 2018, **140**, 3250–3256.
39 S. Ye, C. Ding, M. Liu, A. Wang, Q. Huang and C. Li, *Adv. Mater.*, 2019, **31**, e1902069.
40 Q. Gao, X. Zhang, W. Yin, D. Ma, C. Xie, L. Zheng, X. Dong, L. Mei, J. Yu, C. Wang, Z. Gu and Y. Zhao, *Small*, 2018, **14**, e1802290.
41 L. Wang, B. Zhu, Y. Deng, T. Li, Q. Tian, Z. Yuan, L. Ma, C. Cheng, Q. Guo and L. Qiu, *Adv. Funct. Mater.*, 2021, **31**, 2101804.
42 W. Yin, J. Yu, F. Lv, L. Yan, L. R. Zheng, Z. Gu and Y. Zhao, *ACS Nano*, 2016, **10**, 11000–11011.
43 Y. Zheng, X. Hong, J. Wang, L. Feng, T. Fan, R. Guo and H. Zhang, *Adv. Healthcare Mater.*, 2021, **10**, e2001743.